

## Attractive Dipolar Coupling between Stacked Exciton Fluids


Colin Hubert,<sup>1,\*</sup> Yifat Baruchi,<sup>2,\*</sup> Yotam Mazuz-Harpaz,<sup>2</sup> Kobi Cohen,<sup>2</sup> Klaus Biermann,<sup>1</sup> Mikhail Lemeshko,<sup>3</sup>  
Ken West,<sup>4</sup> Loren Pfeiffer,<sup>4</sup> Ronen Rapaport,<sup>2,†</sup> and Paulo Santos<sup>1,‡</sup>

<sup>1</sup>*Paul-Drude-Institut für Festkörperelektronik, Leibniz-Institut im Forschungsverbund Berlin e. V.,  
Hausvogteiplatz 5-7, 10117 Berlin, Germany*

<sup>2</sup>*The Racah Institute of Physics, The Hebrew University of Jerusalem, Jerusalem 9190401, Israel*

<sup>3</sup>*Institute of Science and Technology Austria, Am Campus 1, 3400 Klosterneuburg, Austria*

<sup>4</sup>*Department of Electrical Engineering, Princeton University, Princeton, New Jersey 08544, USA*

 (Received 26 July 2018; revised manuscript received 5 March 2019; published 8 May 2019)

Dipolar coupling plays a fundamental role in the interaction between electrically or magnetically polarized species such as magnetic atoms and dipolar molecules in a gas or dipolar excitons in the solid state. Unlike Coulomb or contactlike interactions found in many atomic, molecular, and condensed-matter systems, this interaction is long-ranged and highly anisotropic, as it changes from repulsive to attractive depending on the relative positions and orientation of the dipoles. Because of this unique property, many exotic, symmetry-breaking collective states have been recently predicted for cold dipolar gases, but only a few have been experimentally detected and only in dilute atomic dipolar Bose-Einstein condensates. Here, we report on the first observation of attractive dipolar coupling between excitonic dipoles using a new design of stacked semiconductor bilayers. We show that the presence of a dipolar exciton fluid in one bilayer modifies the spatial distribution and increases the binding energy of excitonic dipoles in a vertically remote layer. The binding energy changes are explained using a many-body polaron model describing the deformation of the exciton cloud due to its interaction with a remote dipolar exciton. The surprising nonmonotonic dependence on the cloud density indicates the important role of dipolar correlations, which is unique to dense, strongly interacting dipolar solid-state systems. Our concept provides a route for the realization of dipolar lattices with strong anisotropic interactions in semiconductor systems, which open the way for the observation of theoretically predicted new and exotic collective phases, as well as for engineering and sensing their collective excitations.

DOI: [10.1103/PhysRevX.9.021026](https://doi.org/10.1103/PhysRevX.9.021026)

Subject Areas: Condensed Matter Physics,  
Quantum Physics

### I. INTRODUCTION

The dipolar coupling normally dominates the interaction between charge-neutral species. The characteristic dipolar interaction energy between two dipoles with parallel axes and dipole moments  $\mathbf{p}_1$  and  $\mathbf{p}_2$  in a medium with dielectric constant  $\epsilon$  can be expressed in the far field as

$$U_{dd}(\mathbf{r}) = \frac{p_1 p_2 (1 - 3 \cos^2 \theta)}{4\pi\epsilon\epsilon_0 r^3}, \quad (1)$$

where  $\epsilon_0$  is the vacuum permittivity,  $\theta$  is the angle between  $\mathbf{p}_1$  and  $\mathbf{p}_2$ , and  $\mathbf{r}$  is the vector connecting the dipoles. While

sharing the long decay range of the Coulomb interaction, the dipolar interaction is spatially anisotropic and changes from repulsive to attractive at  $\cos(\theta) = \frac{1}{\sqrt{3}}$ . In natural physical systems containing a large number of dipoles, this anisotropic character gives rise to complex phenomena including self-organization, pattern formation, and instabilities in a wide range of dipolar fluids such as in ferromagnetic or electric fluids [1] as well collective effects in gases or lattices of quantum magnetic [2] or electric dipoles [3]. Fascinating new phases of matter are expected if dipolar interactions are induced into quantum fluids, with an intricate interplay between the attractive and repulsive parts of the interaction and quantum mechanical effects. Among the latter are classical and quantum glasses [4] and novel pair superfluid and supersolid phases [5,6], as well as exotic few-body bound states [7]. On one hand, these new phases may have more than one continuous symmetry simultaneously broken, such as in the prediction of supersolidity. Recent experiments in superfluids of dilute cold atomic species with magnetic dipoles have observed a nonisotropic gas

\*These authors contributed equally.

†ronenr@phys.huji.ac.il

‡santos@pdi-berlin.de

Published by the American Physical Society under the terms of the [Creative Commons Attribution 4.0 International license](https://creativecommons.org/licenses/by/4.0/). Further distribution of this work must maintain attribution to the author(s) and the published article's title, journal citation, and DOI.

expansion and an interaction-driven phase transition between a gas and a state of self-bound, self-ordered liquid droplets, stabilized by the balance between attraction and repulsion and quantum fluctuations [8–11]. On the other hand, long-range dipolar interaction yields the anisotropic intersite coupling required for the study of quantum phase transitions as well as for the simulation of complex spin models in lattices of cold dipolar species [12,13].

While experiments with cold dipolar species largely probe dipolar coupling in the regime of dilute quantum gases and small dipole moments, fluids of electric dipoles in solid-state systems, in particular, spatially indirect dipolar excitons (IXs) in semiconductor bilayers, open up opportunities to explore dipolar coupling in the complementary phase space of high-density, large dipole moments [14–19]. To the best of our knowledge, however, dipolar anisotropy and, in particular, dipolar attraction have never been reported for IX systems, since all studies so far have been conducted in a single dipolar bilayer of aligned IX dipoles, where the dipolar interaction is exclusively repulsive. This repulsive component receives considerable experimental attention in IX systems and is utilized for many optoelectronic functional demonstrations [20–32]. Furthermore, several many-body collective effects related to the bosonic character of IXs in the presence of repulsive interactions are reported [16–19,33–39].

One interesting question is, thus, whether one can also access dipolar attraction in a system of mobile IX dipoles and whether it enables the creation of self-bound states to fully explore dipolar anisotropy. In this work, we demonstrate the dipolar attraction between mobile IX fluids using a novel experimental configuration consisting of stacked IX bilayers. The bilayers are semiconductor double quantum wells (DQWs) (denoted as  $DQW_L$  and  $DQW_H$  in Fig. 1), each consisting of two quantum wells (QWs) separated by a thin barrier [i.e., with a thickness smaller than the exciton Bohr radius; cf. Figs. 1(a) and 1(b)]. A vertical electric field applied across the structure [ $F_z$ ; cf. Fig. 1(a)] drives optically excited electrons and holes to different QWs while maintaining the Coulomb correlation between them. This charge separation induced by  $F_z$  imparts very long lifetimes to the IXs, thus making them quasiequilibrium excitations possessing a large dipole moment, which exceeds the magnitude of atomic and molecular dipoles by several orders of magnitude and gives to strong interparticle interactions [15,40]. The stacked DQW structures result in an attractive inter-DQW dipolar component for a small lateral separation between the IXs. By using spatially resolved spectroscopy, we show that the attractive component of the dipolar interaction induces density correlations between IX fluids in remote DQWs. The latter is analogous to the remote dragging [41] observed in solid-state electron-phonon, electron-electron [42], and electron-hole [42,43] systems but now driven by the attractive dipolar coupling between charge-neutral, bosonic species.

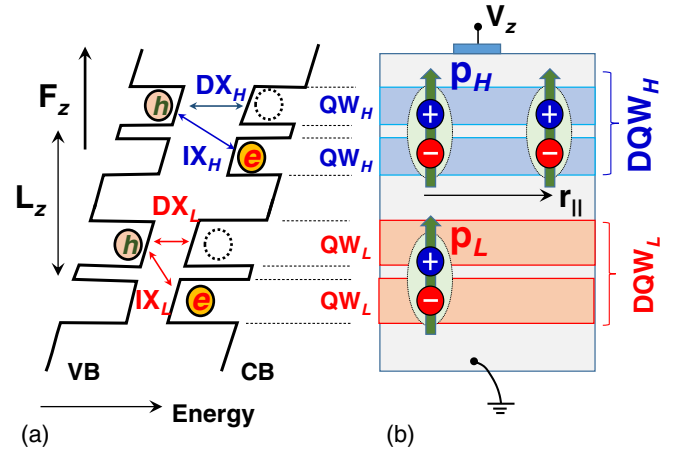


FIG. 1. Interactions between indirect (or dipolar) excitons ( $IX_i$ 's,  $i = L, H$ ) in a sample with coupled double quantum wells (DQW $_i$ 's). (a) Energy diagram and (b) layer structure of the (Al,Ga)As sample. Each DQW consists of two GaAs QWs separated by thin tunneling barriers. A 10-nm-thick (Al,Ga)As barrier between the DQWs prevents carrier tunneling between them. The transverse electric field  $F_z$  bends the conduction (CB) and valence bands (VB). Under laser excitation, the spatial separation between electrons ( $e$ ) and holes ( $h$ ) in each DQW creates  $IX_i$ 's with an electric dipole moment  $p_i$  and reduced energy with respect to intrawell direct excitons ( $DX_i$ 's). The corresponding centers of the DQWs are spaced by  $L_z$ , and the QW pairs in the DQWs have different widths to enable the selective optical excitation of their DX states.

Furthermore, the energetic changes induced by the remote dipolar coupling are nonmonotonic in the fluid density and far exceed the values predicted for the formation of an interbilayer dipolar pair [44]. The large coupling energies are attributed here to a self-bound, collective many-body fluid excitation identified as a dipolar polaron. The latter is analogous to self-bound three-dimensional entities with compensating attraction and repulsion like atomic nuclei, helium, and cold atom droplets. The experimental findings demonstrate the feasibility of the control and manipulation of dipolar species via remote dipolar forces. Furthermore, the sensitivity to the fluid's local correlations opens new ways to study fundamental properties of correlated dipolar fluids.

## II. EXPERIMENTAL CONCEPT

The two closely spaced (Al,Ga)As DQWs are grown by molecular beam epitaxy [cf. Figs. 1(a) and 1(b)] on a GaAs (001) substrate. In order to enable selective optical excitation and detection, the DQWs ( $DQW_L$  and  $DQW_H$ ) have QWs of different thicknesses ( $QW_L$  and  $QW_H$ ), thus resulting in different resonance energies for their direct ( $DX_i$ ) and indirect exciton ( $IX_i$ ) transitions. Here, the subscripts  $i = L, H$  denote DQWs with the higher ( $H$ ) and lower ( $L$ ) excitonic energy. We present experimental results recorded at 2 K on two samples (samples A and B; details about

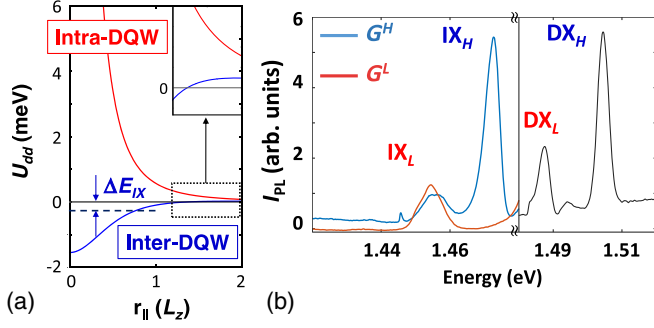


FIG. 2. Interaction potential between indirect excitons (IXs) and their excitation spectra (a) intra- (red curve) and inter-DQW (blue curve) dipolar interaction energy  $U_{dd}(r)$ , for a pair of IXs as a function of the lateral IX-IX separation  $r_{||}$  calculated from Eq. (1) for the DQW stack used in the studies. While the intra-DQW interaction is always repulsive, the inter-DQW one becomes attractive for  $r_{||} < \sqrt{3}L_z$  and forms an IX-IX bound state with the indicated binding energy  $|\Delta E_{IX}|$  [44]. Here,  $L_z$  is the vertical separation between the DQWs. (b) Photoluminescence (PL) spectra of the indirect (left) and direct (right) exciton transitions. The IX transitions on the left are recorded under resonant excitation of their corresponding direct exciton transitions (right) using laser beams  $G^L$  and  $G^H$ , respectively.

both sample structures can be found in the Appendix A), both with QW widths of 10 and 12 nm for  $QW_H$  and  $QW_L$ , respectively, and inter-QW spacing consisting of a 4-nm-thick  $Al_{0.33}Ga_{0.67}As$  barrier. The 10-nm-thick

$Al_{0.33}Ga_{0.67}As$  spacer layer between the DQWs prevents carrier tunneling, which would effectively result in the annihilation of the IXs. Figure 2(a) shows the intra- and inter-DQW dipolar potentials calculated for these structures using Eq. (1). Note that the latter becomes attractive for a small lateral separation between the particles.

The two different QW thicknesses enable selective excitation and detection of IXs in each of the DQWs, as illustrated by the photoluminescence (PL) spectra in Fig. 2(b) and the excitation diagrams in Fig. 3(a). If one neglects the very small absorption cross section of indirect transitions, a laser beam  $G^L$  tuned to the  $DX_L$  resonance excites only  $IX_L$ 's in  $DQW_L$  (throughout the paper, superscripts  $j = L, H, L + H$  denote excitation by laser beams  $G^L$ ,  $G^H$ , and both, respectively). Since the  $DX_L$  lies energetically below  $DX_H$ , a second laser  $G^H$  tuned to  $DX_H$  preferentially excites  $IX_H$ 's in  $DQW_H$  but also creates residual  $IX_L$ 's in the neighboring DQW. One can, nevertheless, achieve a high excitation selectivity of  $IX_H$ 's. In fact, from the ratio between the PL intensities, we estimate that  $G^H$  excites  $DX_H$  densities that are approximately 3.6 times higher than the  $DX_L$  ones.

The PL experiments are carried out by exciting the sample with laser beams  $G^L$  and  $G^H$  with independently adjusted spot sizes and intensities [cf. Fig. 3(a)]. The interaction between the photoexcited exciton clouds is probed by mapping the PL intensities  $I_i^j(x, y)$  with micrometer spatial resolution. The photoexcited IX densities,

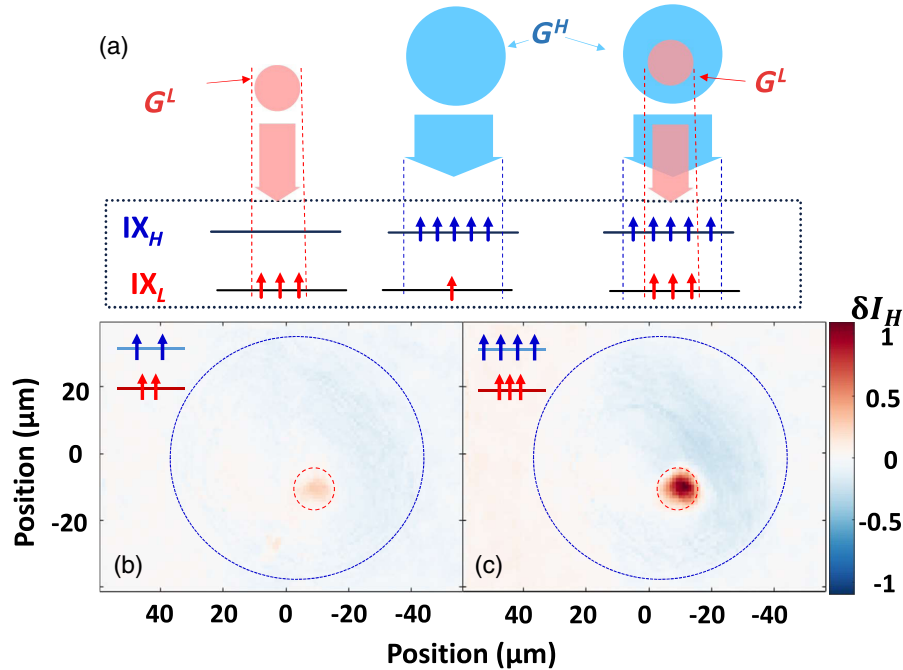


FIG. 3. Optical detection of inter-DQW interactions. (a) Excitation schemes used in the experiments. IX clouds with different diameters are resonantly excited by laser beams  $G^L$  and  $G^H$  tuned to the direct exciton transitions  $DX_L$  and  $DX_H$  of the DQWs. The emission from IX in the two DQWs is spectrally analyzed and detected with spatial resolution. (b),(c) Maps of the relative change  $\delta I_H(x, y)$  in the PL intensity of an  $IX_H$  cloud induced by a narrow  $IX_L$  cloud (marked by the dashed circle) for a fixed  $G^L$  intensity and estimated  $IX_H$  densities at the center of  $G^H$  of (b)  $2.1 \times 10^{10}$  and (c)  $4.6 \times 10^{10} \text{ cm}^{-2}$ , respectively.

typically in the range between  $10^9$  and  $10^{11}$   $\text{cm}^{-2}$ , are determined from the blueshifts of the emission lines in the uncoupled systems after the correction for correlation effects following the procedure depicted in Ref. [15] (cf. Appendix B).

### III. EXPERIMENTAL RESULTS

#### A. Spatially resolved photoluminescence

The attractive inter-DQW interactions can be directly visualized by detecting intensity changes  $\Delta I_i(x, y)$  in PL maps of a probing excitonic cloud in one of the DQWs induced by a perturbing cloud excited in the other DQW [cf. Fig. 3(a)].  $\Delta I_i(x, y)$  is quantified according to

$$\Delta I_i(x, y) = I_i^{L+H}(x, y) - [I_i^H(x, y) + I_i^L(x, y)], \quad i=L, H. \quad (2)$$

Here, the term within the brackets on the rhs accounts for the direct generation of IXs in the probing cloud by each of the laser beams. The most sensitive approach to access inter-DQW interactions consists in detecting  $\Delta I_H(x, y)$ : Since the perturbing laser  $G_L$  does not directly excite  $\text{IX}_H$ , one obtains  $\Delta I_H(x, y) \approx I_H^{L+H}(x, y) - I_H^H(x, y)$ .

Figures 3(b) and 3(c) display maps of the relative changes  $\delta I_H(x, y) = \Delta I_H(x, y)/I_H^H(x, y)$  in the PL intensity of an extended  $\text{IX}_H$  probing cloud induced by a perturbing  $\text{IX}_L$  cloud in sample A. The probing cloud has a diameter of  $60 \mu\text{m}$  (cf. the blue dashed circle), while the perturbing  $G^L$  beam excites a  $20\text{-}\mu\text{m}$ -wide  $\text{IX}_L$  cloud with a density of approximately  $1.1 \times 10^{10} \text{cm}^{-2}$  at its center (cf. the red dashed circle). This perturbing  $\text{IX}_L$  cloud induces a local increase in the  $\text{IX}_H$  density. The IX optical cross section is negligibly small, so that IXs are created by first creating a DX and then converting to an IX. Thus, the perturbing laser  $G^L$  beam effectively does not excite  $\text{IX}_H$ 's [cf. Fig. 2(b)], and the enhanced emission provides direct evidence for an attractive  $\text{IX}_H$ - $\text{IX}_L$  inter-DQW coupling.

The emission from the probing cloud at the overlapping region of the beams enhances significantly with the IX density. Figure 3(c) displays a PL map recorded by increasing the intensity of  $G^H$  (note that the density of the perturbing cloud also increases due to the absorption of  $G^H$  photons in  $\text{DQW}_L$ ; cf. Fig. 3). Under the higher IX densities, the PL intensity from the  $\text{IX}_H$  cloud doubles in the region of the perturbing beam.

Further insight into the inter-DQW interaction can be gained from cross sections of the PL images across the overlap region of the two clouds, as illustrated in Fig. 4. The left panels correspond to the experimental configuration in Figs. 3(b) and 3(c) with a wide  $\text{IX}_H$  and a narrow  $\text{IX}_L$  cloud (cf. diagrams in the upper part of the figure). The changes in the  $\text{IX}_H$  emission in Fig. 4(a) reproduce the density enhancement within the overlap area of the laser beams. The corresponding differential profile  $\Delta I_H$  in Fig. 4(c) shows that the enhanced concentration of  $\text{IX}_H$

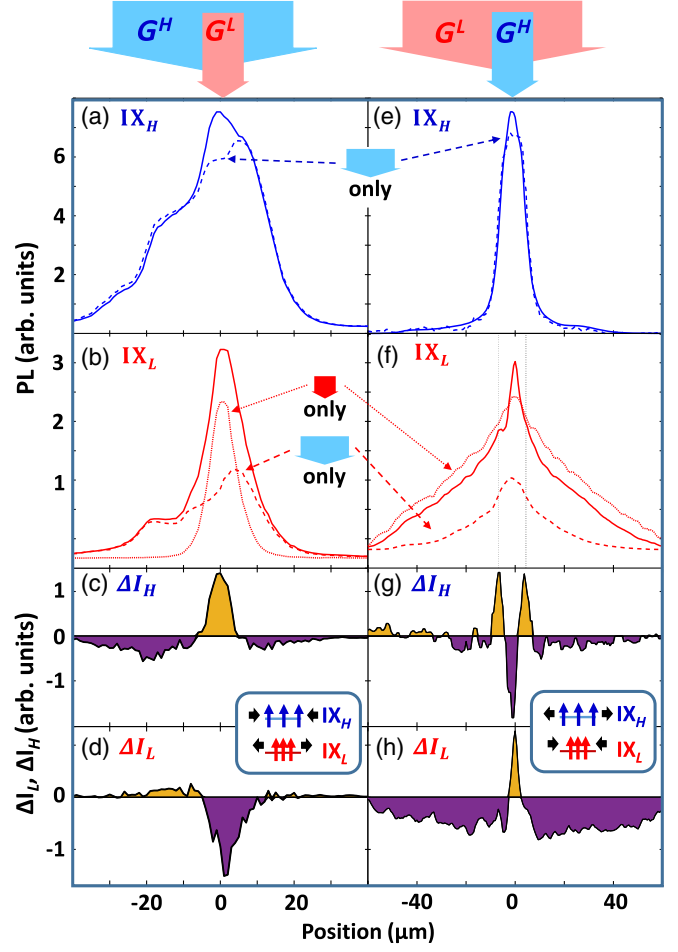


FIG. 4. (a),(b) and (e),(f): Spatially resolved PL intensity of the cross-sectional profiles recorded using the configurations of laser beams sketched on top of each column. The left (right) panels are recorded on sample A (B) using beam widths of 20 (6.5) and  $60 \mu\text{m}$  ( $5.5 \mu\text{m}$ ) for  $G_L$  and  $G_H$ , respectively. (c),(g) and (d),(h): Interaction-induced changes of the  $\text{IX}_H$  ( $\Delta I_H$ ) and  $\text{IX}_L$  ( $\Delta I_L$ ) photoluminescence determined from the above PL cross sections according to Eq. (2). The insets depict the expected forces exerted on the two clouds.

within the overlap region is accompanied by a depletion around it. This behavior follows from the fact that the perturbing  $G^L$  beam does not change the overall  $\text{IX}_H$  population. As a consequence, the enhanced concentration at the overlap area must then arise from the  $\text{IX}_H$  flow from the surrounding areas.

The attractive force leading to the enhanced  $\text{IX}_H$  density should be accompanied by a backaction force on the perturbing  $\text{IX}_L$  cloud [cf. the inset in Fig. 4(c)]. In order to extract information about this backaction effect on the  $\text{IX}_L$  profiles, one needs to account for the fact that  $\text{IX}_L$ 's are also excited by the  $G^H$  beam [cf. Figs. 3(a) and 4(b)], thus leading to a nonvanishing  $I_L^H(x, y)$  term on the rhs in Eq. (2). The intensity variation  $\Delta I_L(x, y)$  calculated from this equation and displayed in Fig. 4(d) shows indeed a



depletion of the  $IX_L$  density around the beam overlap region induced by the remote interaction.

The reciprocal of the above effect is expected if the previous experiment is carried out using a narrow  $G^H$  spot to perturb an  $IX_L$  cloud excited by an extended  $G^L$  beam. Qualitatively similar results are indeed obtained in this situation, as illustrated by the right panels in Fig. 4 (here, smaller laser spots relative to the right panel are employed with diameters of 6.5 and 5.5  $\mu\text{m}$  for  $G^L$  and  $G^H$ , respectively). Since the mobility of  $IX_L$  is much larger than that of the  $IX_H$  [45], the density disturbance of the  $IX_L$  is far more extended than that of the  $IX_H$ , as is seen from the comparison of Figs. 4(c) and 4(g) to Figs. 4(d) and 4(h).

The integrated intensity of the  $\Delta I_H$  curves in Figs. 4(c) and 4(g), which corresponds to the change of the  $IX_H$  population under  $G^L$ , approximately vanishes within the experimental error. For  $IX_L$ 's [cf. Figs. 4(d) and 4(h)], in contrast, the intensity balance determined from Eq. (2) shows not only an extended redistribution but also an overall emission reduction under the perturbing  $G^H$  beam. This emission reduction implies that the proportionality between optical excitation, optical emission, and IX densities does not strictly hold in all situations. This result is, in fact, expected, as shifts of the IX populations across the sample induce significant energy shifts, as is shown in the next section, leading to local variations of the IX lifetimes [46] and, thus, to changes in the relation between the PL intensity and density across the measurement area.

### B. Spectrally resolved photoluminescence

The attraction between the remote IX clouds should be accompanied by changes in the observed IX energies within the overlapping regions of the two beams. The solid lines in Fig. 5 summarize the dependence of the  $IX_L$  (lower curves) and  $IX_H$  (upper curves) energies recorded in sample *B* by fixing the  $IX_H$  density and progressively increasing the density of  $IX_L$  species (stated in terms of the  $G^L$  laser flux). The different curves correspond to different electric fields applied across the structure. The latter controls the IX energies as well as the IX densities in both DQWs (generally, larger electric fields correspond to larger steady-state densities for the same excitation power [46]).

For all applied fields, the energies of both the  $IX_L$  and  $IX_H$  resonances show a pronounced minimum for  $G^L$  powers between 0 and 10  $\mu\text{W}$  followed by a smooth increase in energy for higher  $IX_L$  excitation powers. For each applied electric field, the total  $IX_H$  population remains constant while  $G^L$  increases the  $IX_L$  population. Strikingly, the minima appear only when both species are present and have similar amplitudes for  $IX_L$  and  $IX_H$ . In fact, the energy profiles for the  $IX_L$  species recorded under resonant excitation by solely  $G^L$  (dashed lines) show only the characteristic energy increase associated with the repulsive intra-DQW IX-IX interactions. The nonmonotonicity of the

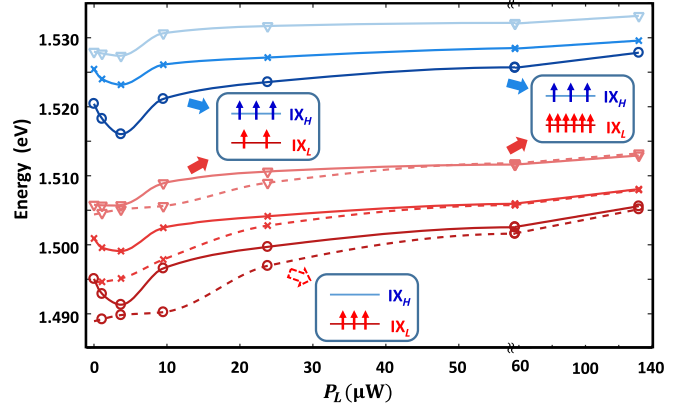


FIG. 5. IX resonance energies as a function of the  $G^L$  excitation power recorded for a constant  $G^H$  power density of 3.6  $\text{W}/\text{cm}^2$ . The symbols correspond to electric fields of 19 (triangles), 25.3 (crosses), and 28.5  $\text{kV}/\text{cm}$  (circles) applied in reverse bias across sample *B*. The solid lines are recorded in the presence of both the  $IX_H$  and  $IX_L$  clouds, while the dashed lines show the  $IX_L$ 's energies detected in the absence of the  $IX_H$  cloud. The lines connecting the measurements (symbols) are spline interpolations.

energy changes in the low  $P_L$  range in Fig. 5 cannot be explained by field screening in the  $\text{DQW}_L$  due to a high  $IX_H$  density. In fact, if the potential across  $\text{DQW}_L$  changes by  $\Delta V_L$ , the expected potential change across  $\text{DQW}_H$  will be given by  $\Delta V_H \sim -\Delta V_L d_{\text{DQW}}/d_T$ , where  $d_{\text{DQW}}$  and  $d_T$  denote the thickness of the DQWs and of the structure, respectively, which implies an energy shift of opposite signs, contrary to our observations. Furthermore, since  $d_{\text{DQW}} \gg d_T$ ,  $\Delta V_L$  is vanishingly small. Screening can thus account neither for the magnitude nor for the nonmonotonic dependence of the energy dips for both  $IX_L$  and  $IX_H$ . This nonmonotonicity as well as the simultaneous energy redshift for  $IX_L$  and  $IX_H$  are rather indicative of attractive inter-DQW interaction. They appear for  $G^L$  laser powers within a relatively small range and essentially vanish at high  $IX_L$  densities, where the IX energy becomes equal to the uncoupled case (dashed lines).

### C. The dipolar-polaron model

The experiments described above provide evidence for an attractive dipolar interaction between IX clouds located in stacked DQWs. The inter-DQW interaction also induces density-dependent energetic shifts (cf. Fig. 5), which are quantified by an inter-DQW binding energy  $\Delta E_{\text{IX}}$  defined as the difference between the IX energies with and without inter-DQW interactions, both referenced at the same IX density. The dependence of  $\Delta E_{\text{IX}}$  for the  $IX_H$  cloud on the perturbing  $IX_L$  density  $n_{\text{IX}}$  is summarized in Fig. 6. The  $n_{\text{IX}}$  values for the different  $G^L$  laser powers and applied fields are extracted from the data in Fig. 5 following the procedure delineated in Appendix B.

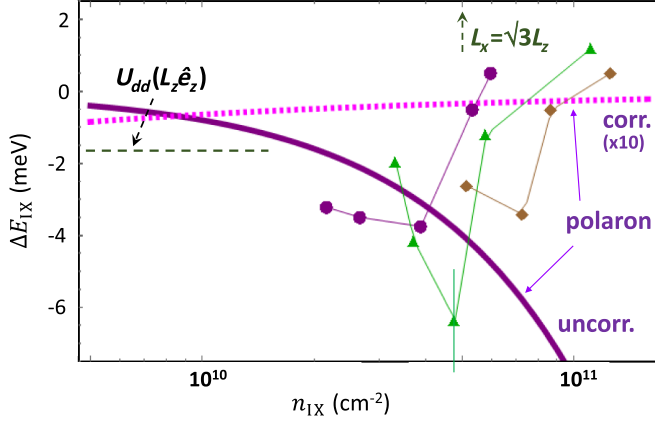


FIG. 6. Interaction-induced energy shifts  $\Delta E_{IX}$  of  $IX_H$  excitons induced by a remote  $IX_L$  cloud with different densities  $n_{IX}$ . Results are shown for probing  $IX_H$  densities estimated as  $8 \times 10^{10}$  (dots),  $9 \times 10^{10}$  (triangles), and  $9.7 \times 10^{10} \text{ cm}^{-2}$  (diamonds). The error bar shown only for  $n_{IX} = 5 \times 10^{10} \text{ cm}^{-2}$  applies for all data points. The vertical dashed arrow marks the density for which  $L_x = \sqrt{3} L_z$ , where  $L_x$  is the average inter- $IX_L$  distance. The thick dotted and solid lines display the prediction of the polaron model (cf. Fig. 7) in the limit of fully correlated [corr.; cf. Eq. (4)] and uncorrelated [uncorr.; cf. Eq. (5)] IX gases, respectively. The horizontal dashed line marks the minimum of the inter-DQW interaction potential  $U_{dd}(L_z \hat{e}_z + r_{||} \hat{e}_{||})$  given by Eq. (1).

The three sets of experimental data points in Fig. 6 correspond to the three different fixed  $IX_H$  densities extracted from the datasets in Fig. 5 for the three different applied electric fields (the associated estimated probing  $IX_H$  densities are listed in the figure caption).

Surprisingly, the maximal observed energy shifts are very large, reaching up to 7 meV. Such large energies are not expected if one considers only the mutual attractive interaction and binding of a pair of IXs, one from each DQW layer. The formation of such bound pairs (“vertical IX molecules”) was recently investigated theoretically by Cohen and co-workers [44]. The inter-DQW dipolar potential calculated for the structures investigated here is illustrated in Fig. 1(c). This attractive potential binds the two IX species into an IX “molecule” with a binding energy  $\Delta E_{IX}$  of only a few tenths of a meV (dashed line in Fig. 1).  $\Delta E_{IX}$  is much smaller than the depth of the potential due to the large zero-point energy corrections arising from the small (reduced) mass of the particles and short spatial extent of the potential. The measured IX energy shifts in Fig. 6 are over an order of magnitude larger than the estimated IX molecular binding energy. These shifts are also significantly larger than the depth of the attractive inter-DQW potential in Fig. 1(c), which is indicated by the horizontal dashed line in Fig. 6 (see a more detailed analysis in Appendix C).

This disagreement between the calculated molecular IX binding energies and the experimental values is not

unexpected, since the large energetic shifts appear for rather high IX densities, for which the average lateral interparticle separation within each layer ( $L_x$ ) becomes comparable to the vertical separation ( $L_z$ ) between the DQWs. Under these conditions, many-body interactions can no longer be neglected. We therefore consider the mutual deformation of the exciton clouds induced by inter-DQW interactions, which may lead to the formation of an IX dipolar polaron. For simplicity, we consider the case where the density in one of the layers is low, so that we can approach the problem as an “impurity problem”: a single IX in  $DQW_2$  interacting with an exciton fluid in  $DQW_1$  (cf. Fig. 7). This approximation, which is described in detail in Appendix D, might still qualitatively capture the case of large IX densities in both layers. We start from a Fröhlich-type polaron Hamiltonian [47]:

$$\hat{H} = \frac{\hat{\mathbf{p}}^2}{2M} + \sum_{\mathbf{k}} \hbar \omega(k) \hat{b}_{\mathbf{k}}^\dagger \hat{b}_{\mathbf{k}} + \sum_{\mathbf{k}} U(k) (e^{-i\mathbf{k}\hat{\mathbf{r}}} \hat{b}_{\mathbf{k}}^\dagger + e^{i\mathbf{k}\hat{\mathbf{r}}} \hat{b}_{\mathbf{k}}), \quad (3)$$

where  $\sum_{\mathbf{k}} = (2\pi)^{-2} \int d^2k$ . The first term describes the “impurity” (i.e., the single IX in  $DQW_2$ ) with momentum  $\hat{\mathbf{p}}$  and mass  $M$ , while the second term gives the kinetic energy of the bosonic bath (e.g., phonons in the exciton liquid formed in  $DQW_1$ ), parametrized by the dispersion relation  $\omega(k)$ . The last term gives the impurity-boson interactions. Here,  $U(k) = f(k)V(k)$ , where  $V(k)$  is the Fourier transform of the two-body interaction potential  $U_{dd}$  in Eq. (1) and  $f(k)$  is a function that depends on the correlation state of the IX gas [cf. Eq. (D3) in Appendix D].

If we consider a static impurity (an “infinite-mass polaron,”  $M = \infty$ , located at  $\mathbf{r} = 0$ ), the Hamiltonian in Eq. (3) can be diagonalized using a coherent-state transformation, yielding a negative “deformation energy”  $\Delta E_{IX}$ , as depicted in Fig. 7. In order to quantitatively estimate  $\Delta E_{IX}$ , we analyze two limiting solutions of Eq. (3) depending on the correlation state of the IX fluid. We first consider a gas of noninteracting IXs with the dispersion relation

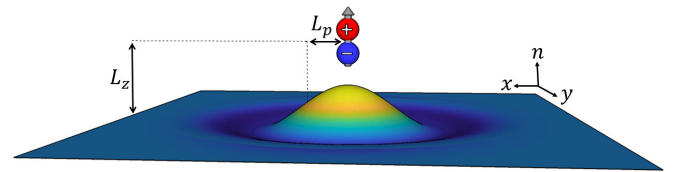


FIG. 7. The polaron model presented here assumes a single IX in the upper layer, interacting with a bath of IXs in the lower layer. The presence of this exciton causes changes in the density distribution of the IX fluid, which can be described as coupled acoustoelectric waves or polarons. The breadth of the polaron,  $L_p$ , is determined by the strength of the interlayer dipolar coupling, which itself is highly dependent on the separation between layers,  $L_z$ .

given by  $\hbar\omega(k) \equiv \varepsilon(k) = \hbar^2 k^2 / (2m)$ , where  $m = m_e + m_{hh}$  is the exciton mass (we take  $m_e = 0.067$  and  $m_{hh} = 0.23$  for the electron and in-plane heavy-hole effective masses in GaAs). In this case, the energy shift becomes

$$\Delta E_{\text{IX}} = -n_{\text{IX}} \mu_1^2 \mu_2^2 \frac{\pi m}{\hbar^2 L_z^2}, \quad (4)$$

where  $\mu_i = p_i / \sqrt{4\pi\epsilon\epsilon_0}$ .

The magenta solid line in Fig. 6 compares the predictions of Eq. (4) with the experimental results for  $\Delta E_{\text{IX}}$ . The model reproduces reasonably well the measured magnitude and density dependence of the shifts in the regime of low to moderate IX fluid densities (i.e., for  $\text{IX}_L$  densities below  $4\text{--}8 \times 10^{10} \text{ cm}^{-2}$ ). This agreement is quite surprising: Equation (4) yields large redshifts, because the expression used for  $\omega(k)$  neglects the additional intra-DQW repulsive interactions arising from the polaron density fluctuation, while the IX fluid at this density range ( $n_{\text{IX}} > 10^{10} \text{ cm}^{-2}$ ) is known to be in a correlated state, where the repulsive interactions play an important role [15,16,34].

The increasing role of intralayer repulsion and dipolar particle correlations within the  $\text{IX}_L$  fluid [15,48] expresses itself in Fig. 5 as a significant reduction of the energy shifts when the  $\text{IX}_L$  densities exceed approximately  $8 \times 10^{10} \text{ cm}^{-2}$ . At this density range, the  $\text{IX}_L$  fluid is expected to be a highly correlated liquid [15,18] with a linear dispersion relation  $\omega(k) \approx c(n_{\text{IX}})k$  determined by a speed of sound  $c(n_{\text{IX}})$ , which, in turn, depends on the density  $n_{\text{IX}}$  [48]. Under such a linear dispersion, the energy shift becomes

$$\Delta E_{\text{IX}} = -n_{\text{IX}} \mu_1^2 \mu_2^2 \frac{3\pi}{8L_z^4 m c^2(n_{\text{IX}})}. \quad (5)$$

Numerical computations by Lozovik *et al.* [48] reveal that the speed of sound for an IX liquid is given by  $c(n_{\text{IX}}) \sim c_0 n_{\text{IX}}^{0.7}$  [cf. Fig. 3(b) in Ref. [48]]. In this case,  $\Delta E_{\text{IX}} \sim n_{\text{IX}}^{-0.4}$  reduces with increasing density. This behavior is reproduced by the thick dotted line in Fig. 6, which is determined from Eq. (5) using the sound velocities from Ref. [48]. It can be shown that the polaron cloud has a Gaussian spatial profile with a Gaussian width  $L_p = 2L_z / \sqrt{35}$  (cf. Appendix E). The decreasing energy shifts with increasing  $n_{\text{IX}}$  can also be understood by the increase stiffness of the IX liquid, which results in a smaller polaron density deformation amplitude.

The polaron binding energies given by Eq. (5) coincide with the reduction of the emission energy of a recombining IX only in the adiabatic approximation, i.e., for interaction processes on a timescale longer than the typical polaron response time,  $\tau_p \approx L_p / c(n_{\text{IX}}) = 3 \text{ ps}$  for  $n_{\text{IX}} = 10^{10} \text{ cm}^{-2}$  and  $0.3 \text{ ps}$  for  $10^{11} \text{ cm}^{-2}$ . Thus it is a good approximation in view of the long IX lifetimes. If, in contrast, the bound single IX recombines within a time shorter than  $\tau_p$ , it will leave the IX fluid in a deformation state described by a Poissonian superposition of an integer number

$n_{\text{ph}} = 0, 1, 2, \dots$  of deformation quanta (“phonons”). The characteristic phonon energy can be determined from the Gaussian polaron profile to be  $|\Delta E_{\text{IX}}^{\text{na}}| = \sqrt{\pi} \hbar c(n_{\text{IX}}) / (2L_p) = 5.5 \text{ meV}$  for  $n_{\text{IX}} = 10^{11} \text{ cm}^{-2}$  (cf. Appendix D). However, for many such recombination events, and if the linewidth is larger than  $|\Delta E_{\text{IX}}^{\text{na}}|$ , the measured redshift will be given by their average:  $\langle n_{\text{ph}} \rangle |\Delta E_{\text{IX}}^{\text{na}}|$ . Calculating  $\langle n_{\text{ph}} \rangle$  within the liquid approximation yields an average redshift energy that differs from that predicted by Eq. (5), up to a numerical factor of the order of unity (cf. Appendix F). The good agreement with Eq. (5) proves the robust relation between the polaron binding and the redshift of the IX emission energies.

The crossover from an uncorrelated to a correlated regime should thus significantly reduce the energy shifts at high IX densities. Since the fraction of particles in a correlated state increases with the density, one also expects a reduction of  $\Delta E_{\text{IX}}$  at high densities. This behavior agrees with the reduction of the binding energy observed in cw experiments for densities beyond approximately  $8 \times 10^{10} \text{ cm}^{-2}$ . The polaron model can thus qualitatively reproduce the energy redshifts over a wide density regime.

#### IV. CONCLUSIONS

We have provided experimental evidence for the attractive component of the dipolar interaction between IX dipoles in stacked DQWs by spatially resolved PL spectroscopy. We have shown that the interaction between spatially isolated IX fluids located in stacked DQWs leads to changes in the IX spatial distribution as well as to an increase in the IX-IX interlayer energy  $\Delta E_{\text{IX}}$ . Surprisingly,  $|\Delta E_{\text{IX}}|$  values far exceed those expected from the binding of two IXs in a molecule. The magnitude and qualitative density dependence of  $|\Delta E_{\text{IX}}|$  is well accounted for by a many-body dipolar-polaron model. The presented results are expected to challenge state-of-the-art theoretical models of dipolar quantum liquids; however, further work will be required to quantify the detailed dependence of the polaron binding energy on IX densities. In particular, it is still not understood why we observe large binding energies, which are qualitatively reproduced by the noninteracting polaron picture of Eq. (3), in a density regime where strong intralayer repulsive interactions are expected to suppress the polaron deformations and, hence, its binding energies. The large shifts make it easier to experimentally address the dependence of the interlayer coupling on the IX dipolar length and inter-DQW separation in future experiments. We also note that, in the current experiments, the densities of the  $\text{IX}_H$  fluid were not negligible; therefore, the single-impurity model used here should be extended in order to get a more quantitative comparison to the experimental data.

The strong attractive inter-DQW coupling opens up possibilities to observe new complex many-body phenomena of dipolar quantum fluids in solid-state systems that



now involve the full anisotropic nature of the dipole-dipole interactions. Since IX systems can probe dipolar densities and interaction strengths currently unavailable in atomic realizations, it is expected to reveal new collective effects and phases, the attractive dipolar polaron being a striking example. The sensitivity of the interlayer coupling to intralayer fluid correlations demonstrated here can be used as a sensitive tool to probe intricate particle correlations in interacting quantum condensates. These experiments also demonstrate the feasibility of the dipolar control of an interlayer flow in excitonic devices based on stacked dipolar structures. Concepts for the control of IX flows based on repulsive interactions have previously been put forward [44]. The results presented here enable their extension to attractive potentials, which can be realized using stacked DQW structures. Finally, the present investigations represent a first step towards for the realization in the solid state of dipolar lattices with anisotropic interactions, thus the mimicking optical lattices of cold magnetic [49] or electric dipoles [3] presently proposed for quantum simulation [12,13]. Our work represents only the first, but the crucial, step towards the realization of such phases, which rely on the anisotropy of the dipole-dipole interactions. Furthermore, excitonic liquids allow one to achieve higher dipole densities compared to ultracold gases and, therefore, more pronounced effects.

### ACKNOWLEDGMENTS

The authors thank Stefan Fölsch and Maxim Khodas for fruitful discussions and comments on the manuscript. This research was made possible by the German-Israeli Foundation (GIF) Grant Agreement No. I-1277-303.10/2014 and the Austrian Science Fund (FWF), Project No. P29902-N27. We also acknowledge the support by the Israel Science Foundation, Grant No. 836/17. The work at Princeton University was funded by the Gordon and Betty Moore Foundation through EPiQS initiative Grant No. GBMF4420 and by NSF MRSEC Grant No. DMR-1420541.

### APPENDIX A: SAMPLES

The studies are carried out in two (Al,Ga)As layer structures (samples *A* and *B*) grown by molecular beam epitaxy on GaAs (001) at the Paul-Drude-Institut (sample *A*) and at Princeton University (sample *B*). Both samples have DQWs with the same layer structure, as described in the main text.

For sample *A*, the DQW stack is placed approximately 500 nm away from the semitransparent top gate and only 100 nm above the bottom electrode. The electric field responsible for IX formation is applied between the top gate and this bottom electrode. The short distance between the DQWs and the bottom electrode minimizes coplanar stray electric fields at the edges of the top gate.

This electrode consists of an *n*-type doped distributed Bragg reflector (DBR) consisting of four Al<sub>0.15</sub>Ga<sub>0.85</sub>As and AlAs layer stacks designed for a central wavelength  $\lambda_c = 820$  nm. The DBR enhances the IX emission by backreflecting the photons emitted towards the substrate. In addition, it suppresses the PL from the substrate most notably, the spectral lines related to the GaAs exciton (around 818 nm) and GaAs:C (830 nm) transitions, which overlap with the IX PL spectra.

In sample *B*, the DQW stack is also placed approximately 520 nm away from the top gate but is situated 250 nm away from the bottom electrode. The substrate is *n* doped and used as the back contact in a Schottky-type diode, with the DQWs being again situated in the intrinsic region. The QWs are GaAs, while the intra-DQW barriers are AlAs. The barriers between the substrate and top contact are also Al<sub>0.3</sub>Ga<sub>0.7</sub>As.

The main difference between the two samples is the addition of a Bragg mirror in sample *A*, as well as smaller radial electric fields, due to the placement of the DQWs closer to the (semi-infinite) ground plane. The Bragg mirror increases the captured photoluminescence flux and, therefore, allows the operation of the device at higher electric fields (limited by the breakdown voltage, instead of the photoluminescence flux) so that the IX energies are 30–40 meV lower than the direct excitons.

### APPENDIX B: DETERMINATION OF IX DENSITY

The data shown in Fig. 5 are processed from several individually recorded spectra. The FWHM linewidth of the recorded IX spectra is typically around 2–5 meV, mainly dependent on the density and the integration area. The spectra shown in Fig. 8 (recorded from sample *A*) are typical raw PL data demonstrating the energy shifts induced by the inter-DQW interactions. The energies used in Fig. 5 (recorded from sample *B*) are determined from the peak energies and intensities obtained from such spectra using the procedure described below.

In instances where the diffusion of the IX clouds results in pronounced energy shifts, the energy at the position of highest density is used.

The exact calibration of the exciton density in such systems is a well-known challenge [34]. Here, we use the following procedure: For every experiment with a given applied bias, we use the experiment with only the  $G^L$  laser as a reference. Since this laser creates only a population of  $IX_L$ , the interactions in this case are only repulsive, leading to a blueshift of the energy with increasing laser power (increasing density). We then choose a point that has an interaction energy well within the range expected for a correlated liquid regime, described in detail in Ref. [15]. We then use Eq. (5.5) in that reference to estimate the density of  $IX_L$ 's for this experimental point. The IX densities of both  $IX_L$  and  $IX_H$  can then be deduced relative



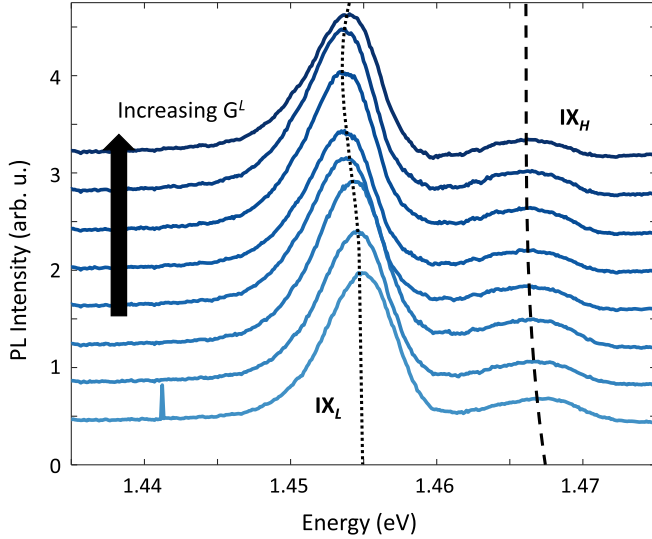


FIG. 8. Spatially integrated PL spectra for the  $IX_L$  (around 1.455 eV) and  $IX_H$  (around 1.468 eV) resonances as a function of the  $IX_L$  excitation power  $G^L$  (from bottom to top:  $G^L = 0$  (lightest), 10, 20, 30, 43, 55, 80, 130 (darkest)  $\mu\text{W}$ ). The electric field is 38 kV/cm and  $G^H = 40 \mu\text{W}$ . Data is taken from sample A, but is the equivalent experiment for sample B shown in Fig. 5 of the main text. Each integrated spectrum is normalized with respect to its maximum intensity to allow easy comparison of the energetic red shifts with increasing  $IX_L$  intensity. The energy of the  $IX_L$  and  $IX_H$  transitions are marked by the dot and dashed lines, respectively. Each of these spectrum would be equivalent to a single data point in Fig. 5.

to this reference density by comparing the relative emission intensities of each of the IX species to the emission intensity of the reference point, using the procedure developed in Refs. [16,46]. Here, it is shown that the emission intensity of the IX  $I_i \propto n_i/\tau_i$ , where  $n_i$  is the  $IX_i$  density and  $\tau_i$  is the IX lifetime. This lifetime is shown in Ref. [46] to be related to the energy difference between the IX emission and the DX emission energies:

$$\tau = c_d(\Delta E_{\text{DX-IX}})^2, \quad (\text{B1})$$

where  $\Delta E_{\text{DX-IX}} = E_{\text{DX}} - E_{\text{IX}}$  and the proportionality factor  $c_d$  depends on the layer structure of the sample and the applied bias but does not depend on the density over a rather wide range of densities. Thus, for every two points with the same applied bias but different laser excitation powers, the ratio between their corresponding IX densities can be found using

$$\frac{n^{(1)}}{n^{(2)}} = \frac{\tau^{(1)} I_{\text{PL}}^{(1)}}{\tau^{(2)} I_{\text{PL}}^{(2)}} = \frac{I_{\text{PL}}^{(1)}}{I_{\text{PL}}^{(2)}} \left[ \frac{\Delta E_{\text{DX-IX}}^{(1)}}{\Delta E_{\text{DX-IX}}^{(2)}} \right]^2. \quad (\text{B2})$$

This ratio is used to calibrate the absolute density of all experimental points in any given experiment with

a fixed applied bias to the reference point in that experiment.

### APPENDIX C: ELECTROSTATIC CONTRIBUTIONS

The inter-DQW potential in Fig. 1(c) of the main text applies for the inter-DQW interaction between two aligned dipoles, each in one of the DQWs. In this section, we estimate the dependence of the inter-DQW potential  $V_{\text{lat}}$  on the density of particles. For that purpose, we calculate the dipolar potential experienced by a single IX in DQW<sub>2</sub> due to the coupling to an excitonic cloud in DQW<sub>1</sub> (cf. the inset in Fig. 9) by (i) neglecting kinetic effects and (ii) assuming that the IXs within the cloud of DQW<sub>1</sub> are arranged in a closed-packed triangular lattice with lattice constant  $L_x$  [50].  $V_{\text{lat}}(\mathbf{r})$  is determined by summing the two-particle contributions  $U_{dd}(r)$  [cf. Eq. (1)] over a large number of lattice lattices.

The shaded region in Fig. 9 marks the range of energies spanned by  $V_{\text{lat}}(\mathbf{r})$  as the single IX (with coordinate  $\mathbf{r}$ ) moves relative to the lattice, calculated for different lattice densities. For densities yielding  $L_x \gg L_z$ , the lattice potential around each site resembles the one for  $U_{dd}$  in Fig. 1(c) of the main text and indicated by the dashed horizontal line in Fig. 6. As  $L_x$  decreases to values comparable to  $L_z$ , the minima of  $V_{\text{lat}}(\mathbf{r})$  remain aligned with the lattice sites. In the opposite limit  $L_x \ll L_z$ ,  $V_{\text{lat}}(\mathbf{r}) \rightarrow 0$ , thus reproducing the fact that the electric field generated by an infinite sheet of dipoles vanishes at large distances. The minimum values for  $V_{\text{lat}}(\mathbf{r})$  are always larger than the minimum for the IX-molecule interaction potential  $U_{dd}$ . This simple model for the interaction underestimates the measured binding energies  $|\Delta E_{\text{IX}}|$  indicated by the symbols in Fig. 6 in the main text.

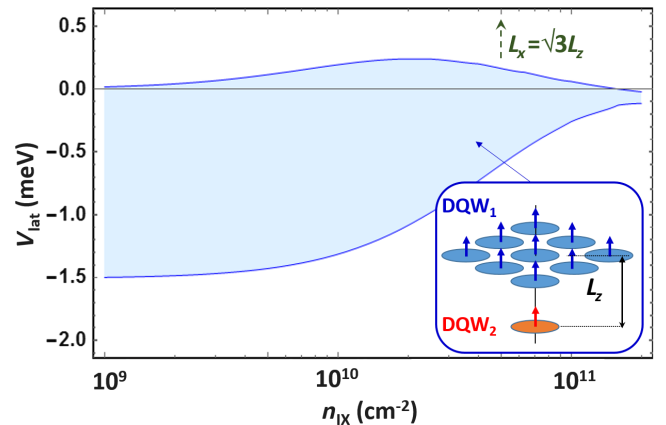


FIG. 9. Range of energies (shaded region) spanned by the inter-DQW interaction between a single IX in DQW<sub>2</sub> and a closed-packed triangular lattice of IXs with density  $n_{\text{IX}}$  in DQW<sub>1</sub>, as illustrated in the inset.  $n_{\text{IX}}$  is related to the triangular lattice constant  $L_x$  by  $n_{\text{IX}} = [2/(\sqrt{3}L_x^2)]$ .

## APPENDIX D: POLARON MODEL

We consider two layers of excitons with dipole moments  $\mu_{1,2} = p_{1,2}/\sqrt{4\pi\epsilon\epsilon_0} = ed_{1,2}/\sqrt{4\pi\epsilon\epsilon_0}$ , separated by a distance  $L_z$ . We treat excitons as point dipoles, which is a good approximation only for  $d_{1,2} \ll L_z$ . In our setup,  $d_{1,2}/L_z \sim 0.3$ ; however, it should still provide a reasonable estimate. The dipole-dipole interaction between the dipole  $\mu_1$  (located at  $\rho = 0$  in DQW<sub>1</sub>) and the dipole  $\mu_2$  (located in DQW<sub>2</sub> at a lateral separation  $\rho$ ) can be written as [cf. Eq. (1)]

$$V(\rho) = \frac{\mu_1\mu_2}{(L_z^2 + \rho^2)^{3/2}} \left(1 - \frac{3L_z^2}{L_z^2 + \rho^2}\right). \quad (\text{D1})$$

This interaction is sign changing, so a net mean-field interaction of a dipole with a dipolar plane vanishes:

$$\int d^2\rho V(\rho) = 0. \quad (\text{D2})$$

In order to solve Eq. (3) of the main text, we first note that the Fourier transform of the two-body interaction potential of Eq. (D1) can be expressed as

$$V(k) = \int d^2\rho V(\rho)e^{-i\mathbf{k}\rho} = -\mu_1\mu_2 2\pi k e^{-kL_z}. \quad (\text{D3})$$

In addition,  $U(k) = f(k)V(k)$ ,  $f(k) = \{n_{\text{IX}}\epsilon(k)/[\hbar\omega(k)]\}^{1/2}$ , is a function that depends on the density  $n_{\text{IX}}$  and single-particle energy  $\epsilon(k) = \hbar^2 k^2/(2m)$  as well as on the correlation state of the IX gas expressed in terms of its dispersion relation  $\hbar\omega(k)$ .

If we consider a static impurity (an ‘‘infinite-mass polaron,’’  $M = \infty$ , located at  $\mathbf{r} = 0$ ), the Hamiltonian (3) can be diagonalized using a coherent-state transformation:

$$\hat{S} = \exp\left[-\sum_{\mathbf{k}} \frac{U(k)}{\hbar\omega(k)} (\hat{b}_{\mathbf{k}}^\dagger - \hat{b}_{\mathbf{k}})\right], \quad (\text{D4})$$

which gives the following ground-state energy shift:

$$\Delta E = -\sum_{\mathbf{k}} \frac{U(k)^2}{\hbar\omega(k)} \quad (\text{D5})$$

(the ground state is given by  $|\psi\rangle = \hat{S}|0\rangle$ ).

One can see that  $\Delta E$  is always negative: This result is a general property of Hamiltonians with linear coupling, such as Eq. (3). The energy shifts for a gas of noninteracting excitons expressed by Eq. (4) in the main text are obtained by integrating Eq. (D5) using the dispersion relation is given by  $\hbar\omega(k) \equiv \epsilon(k)$ . The corresponding expression for an interacting exciton gas [Eq. (5) in the main text] is determined in the same way using a dispersion

relation  $\omega(k) \approx c(n_{\text{IX}})k$ , where  $c(n_{\text{IX}})$  is the density-dependent speed of sound.

## APPENDIX E: POLARON DENSITY PROFILES

In real space, the density deformation of DQW<sub>1</sub> is given by  $\Delta n_{\text{IX}}(\rho) = \langle\psi|\hat{b}_{\mathbf{r}}^\dagger\hat{b}_{\mathbf{r}}|\psi\rangle$ , where  $\hat{b}_{\mathbf{r}}^\dagger = \int d^2k/(2\pi)^2 \hat{b}_{\mathbf{k}}^\dagger e^{i\mathbf{k}\rho}$ . In the case of a correlated exciton in DQW<sub>1</sub>, the density deformation can be approximated by a Gaussian at small values of  $\rho$ :

$$\Delta n_{\text{IX}}(\rho) = n_{\text{IX}} \frac{\mu_1^2\mu_2^2}{2\hbar mc^3(n_{\text{IX}})} \frac{9\pi}{16L_z^5} e^{-(\rho^2/2L_p^2)}, \quad (\text{E1})$$

where  $L_p = 2L_z/\sqrt{35}$ . By integrating  $\Delta n_{\text{IX}}$  over the DQW plane, one obtains a total density excess corresponding to approximately 0.1 particles for  $n_{\text{IX}} = 10^{10} \text{ cm}^{-2}$ .

## APPENDIX F: NONADIABATIC ENERGY SHIFTS

The polaron wave function is  $|\psi\rangle = \sum_{\mathbf{q}} F(\mathbf{q}) \hat{b}_{\mathbf{r}}^\dagger |0\rangle = \sum_{\mathbf{q}} F(\mathbf{q}) |\mathbf{q}\rangle$ , where  $F(\mathbf{q})$  is the Fourier transform of the Gaussian real space profile with width  $L_p$  [cf. Eq. (E1)]. For a state having a single polaron quantum (‘‘phonon’’), the normalization condition  $\sum_{\mathbf{q}',\mathbf{q}''} \langle\mathbf{q}'|\mathbf{F}^*(\mathbf{q}')\mathbf{F}(\mathbf{q}'')|\mathbf{q}''\rangle$  yields  $F(\mathbf{q}) = \sqrt{8mL_p^2} e^{-\rho^2/2L_p^2}$ . The single phonon energy can be determined by replacing  $\omega(\mathbf{q}) \approx c(n_{\text{IX}})q$  in the following expression:

$$|\Delta E_{\text{IX}}^{\text{na}}| = \langle\psi|\hbar\omega(\mathbf{q})|\psi\rangle = \frac{\sqrt{\pi}\hbar c(n_{\text{IX}})}{2L_p}. \quad (\text{F1})$$

This expression yields  $|\Delta E_{\text{IX}}^{\text{na}}| = 1.1 \text{ meV}$  for  $n_{\text{IX}} = 10^{10} \text{ cm}^{-2}$  and  $5.5 \text{ meV}$  for  $n_{\text{IX}} = 10^{11} \text{ cm}^{-2}$ .

The average phonon energy, which corresponds to the redshift and broadening of a bound IX in the nonadiabatic approximation, can then be calculated according to

$$\langle n_{\text{ph}} \rangle |\Delta E_{\text{IX}}^{\text{na}}| = |\Delta E_{\text{IX}}^{\text{na}}| \int d\rho^2 \Delta n_{\text{IX}}(\rho) \quad (\text{F2})$$

$$= -f^{\text{na}} n_{\text{IX}} \mu_1^2 \mu_2^2 \frac{3\pi}{8L_z^4 m c^2(n_{\text{IX}})}. \quad (\text{F3})$$

This expression is similar to Eq. (5) in the main text, exception for a prefactor  $f^{\text{na}} = 3\pi^{3/2}/4 \sim 1.4$ . The density-dependent shifts are comparable to the ones determined in the adiabatic approximation.

[1] T. Lahaye, T. Koch, B. Frohlich, M. Fattori, J. Metz, A. Griesmaier, S. Giovanazzi, and T. Pfau, *Strong Dipolar Effects in a Quantum Ferrofluid*, *Nature (London)* **448**, 672 (2007).

- [2] A. de Paz, A. Sharma, A. Chotia, E. Maréchal, J. H. Huckans, P. Pedri, L. Santos, O. Gorceix, L. Vernac, and B. Laburthe-Tolra, *Nonequilibrium Quantum Magnetism in a Dipolar Lattice Gas*, *Phys. Rev. Lett.* **111**, 185305 (2013).
- [3] K.-K. Ni, S. Ospelkaus, M. H. G. de Miranda, A. Pe'er, B. Neyenhuis, J. J. Zirbel, S. Kotochigova, P. S. Julienne, D. S. Jin, and J. Ye, *A High Phase-Space-Density Gas of Polar Molecules*, *Science* **322**, 231 (2008).
- [4] W. Lechner and P. Zoller, *From Classical to Quantum Glasses with Ultracold Polar Molecules*, *Phys. Rev. Lett.* **111**, 185306 (2013).
- [5] A. Safavi-Naini, S. G. Söyler, G. Pupillo, H. R. Sadeghpour, and B. Capogrosso-Sansone, *Quantum Phases of Dipolar Bosons in Bilayer Geometry*, *New J. Phys.* **15**, 013036 (2013).
- [6] A. Macia, G. E. Astrakharchik, F. Mazzanti, S. Giorgini, and J. Boronat, *Single-Particle versus Pair Superfluidity in a Bilayer System of Dipolar Bosons*, *Phys. Rev. A* **90**, 043623 (2014).
- [7] B. Wunsch, N. T. Zinner, I. B. Mekhov, S.-J. Huang, D.-W. Wang, and E. Demler, *Few-Body Bound States in Dipolar Gases and Their Detection*, *Phys. Rev. Lett.* **107**, 073201 (2011).
- [8] T. Lahaye, C. Menotti, L. Santos, M. Lewenstein, and T. Pfau, *The Physics of Dipolar Bosonic Quantum Gases*, *Rep. Prog. Phys.* **72**, 126401 (2009).
- [9] I. Ferrier-Barbut, H. Kadau, M. Schmitt, M. Wenzel, and T. Pfau, *Observation of Quantum Droplets in a Strongly Dipolar Bose Gas*, *Phys. Rev. Lett.* **116**, 215301 (2016).
- [10] H. Kadau, M. Schmitt, M. Wenzel, C. Wink, T. Maier, I. Ferrier-Barbut, and T. Pfau, *Observing the Rosensweig Instability of a Quantum Ferrofluid*, *Nature (London)* **530**, 194 (2016).
- [11] L. Chomaz, S. Baier, D. Petter, M. J. Mark, F. Wächtler, L. Santos, and F. Ferlaino, *Quantum-Fluctuation-Driven Crossover from a Dilute Bose-Einstein Condensate to a Macrodroplet in a Dipolar Quantum Fluid*, *Phys. Rev. X* **6**, 041039 (2016).
- [12] I. M. Georgescu, S. Ashhab, and F. Nori, *Quantum Simulation*, *Rev. Mod. Phys.* **86**, 153 (2014).
- [13] C. Gross and I. Bloch, *Quantum Simulations with Ultracold Atoms in Optical Lattices*, *Science* **357**, 995 (2017).
- [14] G. Chen, R. Rapaport, L. N. Pfeiffer, K. West, P. M. Platzman, S. Simon, Z. Vörös, and D. Snoke, *Artificial Trapping of a Stable High-Density Dipolar Exciton Fluid*, *Phys. Rev. B* **74**, 045309 (2006).
- [15] B. Laikhtman and R. Rapaport, *Exciton Correlations in Coupled Quantum Wells and Their Luminescence Blue Shift*, *Phys. Rev. B* **80**, 195313 (2009).
- [16] Y. Shilo, K. Cohen, B. Laikhtman, K. West, L. Pfeiffer, and R. Rapaport, *Particle Correlations and Evidence for Dark State Condensation in a Cold Dipolar Exciton Fluid*, *Nat. Commun.* **4**, 2335 (2013).
- [17] S. Misra, M. Stern, A. Joshua, V. Umansky, and I. Bar-Joseph, *Experimental Study of the Exciton Gas-Liquid Transition in Coupled Quantum Wells*, *Phys. Rev. Lett.* **120**, 047402 (2018).
- [18] M. Stern, V. Umansky, and I. Bar-Joseph, *Exciton Liquid in Coupled Quantum Wells*, *Science* **343**, 55 (2014).
- [19] Y. Mazuz-Harpaz, M. Khodas, and R. Rapaport, *Dynamical Formation and Interaction-Induced Stabilization of Dark Condensates of Dipolar Excitons*, [arXiv:1803.03918](https://arxiv.org/abs/1803.03918).
- [20] G. J. Schinner, J. Repp, E. Schubert, A. K. Rai, D. Reuter, A. D. Wieck, A. O. Govorov, A. W. Holleitner, and J. P. Kotthaus, *Confinement and Interaction of Single Indirect Excitons in a Voltage-Controlled Trap Formed inside Double InGaAs Quantum Wells*, *Phys. Rev. Lett.* **110**, 127403 (2013).
- [21] G. J. Schinner, E. Schubert, M. P. Stallhofer, J. P. Kotthaus, D. Schuh, A. K. Rai, D. Reuter, A. D. Wieck, and A. O. Govorov, *Electrostatically Trapping Indirect Excitons in Coupled InXGa1-XAs quantum wells*, *Phys. Rev. B* **83**, 165308 (2011).
- [22] L. P. Kouwenhoven, *Quantized Photocurrent in a Single-Exciton Pump*, *Europhys. Lett.* **18**, 607 (1992).
- [23] M. Alloing, A. Lemaître, E. Galopin, and F. Dubin, *Optically Programmable Excitonic Traps*, *Sci. Rep.* **3**, 1578 (2013).
- [24] A. A. High, E. E. Novitskaya, L. V. Butov, M. Hanson, and A. C. Gossard, *Control of Exciton Fluxes in an Excitonic Integrated Circuit*, *Science* **321**, 229 (2008).
- [25] K. Kowalik-Seidl, X. P. Vögele, B. N. Rimpfl, G. J. Schinner, D. Schuh, W. Wegscheider, A. W. Holleitner, and J. P. Kotthaus, *Tunable Photoemission from an Excitonic Antitrap*, *Nano Lett.* **12**, 326 (2012).
- [26] A. A. High, A. T. Hammack, L. V. Butov, M. Hanson, and A. C. Gossard, *Exciton Optoelectronic Transistor*, *Opt. Lett.* **32**, 2466 (2007).
- [27] G. Grosso, J. Graves, A. T. Hammack, A. High, L. V. Butov, M. Hanson, and A. C. Gossard, *Excitonic Switches Operating at around 100 K*, *Nat. Photonics* **3**, 577 (2009).
- [28] T. Lundstrom, W. Schoenfeld, H. Lee, and P. M. Petroff, *Exciton Storage in Semiconductor Self-Assembled Quantum Dots*, *Science* **286**, 2312 (1999).
- [29] H. J. Krenner, C. E. Pryor, J. He, and P. M. Petroff, *A semiconductor Exciton Memory Cell Based on a Single Quantum Nanostructure*, *Nano Lett.* **8**, 1750 (2008).
- [30] M. Bayer, G. Ortner, A. Larionov, V. Timofeev, A. Forchel, P. Hawrylak, K. Hinzer, M. Korkusinski, S. Fafard, and Z. Wasilewski, *Entangled Exciton States in Quantum Dot Molecules*, *Physica Amsterdam* **12E**, 900 (2002).
- [31] H. S. Borges, L. Sanz, and A. M. Alcalde, *Excitonic Entanglement of Protected States in Quantum Dot Molecules*, *Phys. Lett. A* **380**, 3111 (2016).
- [32] F. Lacava, *Classical Electrodynamics* (Springer, New York, 2016), Chap. Multipolar Expansion of the Electrostatic Potential, pp. 17–31.
- [33] A. A. High, J. R. Leonard, A. T. Hammack, M. M. Fogler, L. V. Butov, A. V. Kavokin, K. L. Campman, and A. C. Gossard, *Spontaneous Coherence in a Cold Exciton Gas*, *Nature (London)* **483**, 584 (2012).
- [34] K. Cohen, Y. Shilo, K. West, L. Pfeiffer, and R. Rapaport, *Dark High Density Dipolar Liquid of Excitons*, *Nano Lett.* **16**, 3726 (2016).
- [35] M. Stern, V. Garmider, V. Umansky, and I. Bar-Joseph, *Mott Transition of Excitons in Coupled Quantum Wells*, *Phys. Rev. Lett.* **100**, 256402 (2008).
- [36] M. Alloing, M. Beian, D. Fuster, Y. Gonzalez, L. Gonzalez, R. Combescot, M. Combescot, and F. Dubin, *Evidence for a*

- Bose-Einstein Condensate of Excitons*, *Europhys. Lett.* **107**, 10012 (2014).
- [37] M. Combescot, R. Combescot, and F. Dubin, *Bose-Einstein Condensation and Indirect Excitons: A Review*, *Rep. Prog. Phys.* **80**, 066501 (2017).
- [38] A. A. Dremin, A. V. Larionov, and V. B. Timofeev, *Bose Condensation of Interwell Excitons in Lateral Traps: A Phase Diagram*, *Phys. Solid State* **46**, 170 (2004).
- [39] X. Zhu, P. B. Littlewood, M. S. Hybertsen, and T. M. Rice, *Exciton Condensate in Semiconductor Quantum Well Structures*, *Phys. Rev. Lett.* **74**, 1633 (1995).
- [40] C. Schindler and R. Zimmermann, *Analysis of the Exciton-Exciton Interaction in Semiconductor Quantum Wells*, *Phys. Rev. B* **78**, 045313 (2008).
- [41] B. N. Narozhny and A. Levchenko, *Coulomb Drag*, *Rev. Mod. Phys.* **88**, 025003 (2016).
- [42] P. M. Solomon, P. J. Price, D. J. Frank, and D. C. La Tulipe, *New Phenomena in Coupled Transport between 2D and 3D Electron-Gas Layers*, *Phys. Rev. Lett.* **63**, 2508 (1989).
- [43] D. Nandi, A. D. K. Finck, J. P. Eisenstein, L. N. Pfeiffer, and K. W. West, *Exciton Condensation and Perfect Coulomb Drag*, *Nature (London)* **488**, 481 (2012).
- [44] K. Cohen, M. Khodas, B. Laikhtman, P. V. Santos, and R. Rapaport, *Vertically Coupled Dipolar Exciton Molecules*, *Phys. Rev. B* **93**, 235310 (2016).
- [45] Z. Vörös, R. Balili, D. W. Snoke, L. Pfeiffer, and K. West, *Long-Distance Diffusion of Excitons in Double Quantum Well Structures*, *Phys. Rev. Lett.* **94**, 226401 (2005).
- [46] Y. Mazuz-Harpaz, K. Cohen, B. Laikhtman, R. Rapaport, K. West, and L. N. Pfeiffer, *Radiative Lifetimes of Dipolar Excitons in Double Quantum Wells*, *Phys. Rev. B* **95**, 155302 (2017).
- [47] J. T. Devreese, *Lectures on Fröhlich Polarons from 3D to 0D—Including Detailed Theoretical Derivations*, [arXiv: 1012.4576v6](https://arxiv.org/abs/1012.4576v6).
- [48] Y. E. Lozovik, I. L. Kurbakov, G. E. Astrakharchik, J. Boronat, and M. Willander, *Strong Correlation Effects in 2d Bose-Einstein Condensed Dipolar Excitons*, *Solid State Commun.* **144**, 399 (2007).
- [49] S. Baier, M. J. Mark, D. Petter, K. Aikawa, L. Chomaz, Z. Cai, M. Baranov, P. Zoller, and F. Ferlaino, *Extended Bose-Hubbard Models with Ultracold Magnetic Atoms*, *Science* **352**, 201 (2016).
- [50] M. Remeika, J. Leonard, C. Dorow, M. Fogler, L. Butov, M. Hanson, and A. Gossard, *Measurement of Exciton Correlations Using Electrostatic Lattices*, in *Proceedings of the Conference on Lasers and Electro-Optics* (Optical Society of America, Washington, DC, 2016), p. JW2A.97.